Raman Spectroscopy, Modeling and Simulation Studies of Carbon Nanotubes

Daniel Casimir, Raul Garcia-Sanchez and Prabhakar Misra

Abstract This chapter focuses on two types of carbon nanotubes (CNTs): single-walled carbon nanotubes (SWCNTs) and multi-walled carbon nanotubes (MWCNTs). CNTs are cylindrically-shaped carbon allotropes. They consist of a single layer of sp^2-hybridized carbon atoms, giving it a hollow cylindrical shape. The majority of SWCNT samples have diameters on the order of ~ 1 nm and lengths on the order of microns to centimeters. MWCNTs are composed of concentric layers of SWCNTs nested inside one another, giving it a layered cylindrical shape. In the present chapter, we will provide a historical overview of CNTs and examine specifically their thermal properties as it relates to their applications to the semiconductor industry and nanoelectronics. The understanding of CNT chirality through the visualization of rolled-up graphene sheets will provide insight into the versatility and myriad thermo-mechanical and electrical properties of CNTs. We will focus on the use of Raman spectroscopy and Molecular Dynamics (MD) simulations to characterize and investigate the thermal characteristics of SWCNTs.

Keywords Carbon nanotubes · Single-walled · Multi-walled · Chirality · Thermal properties · Thermo-mechanical properties · Electrical properties · Graphene · Raman spectroscopy · Modeling · Molecular Dynamics (MD) simulation

1 Introduction

In order to provide an overview of carbon nanotubes, we will take the historical perspective, although the reported timeline has been mired in controversy. In 1952, Soviet scientists, Radushkevich and Lukyanovich reported the first Transmission Electron Microscope (TEM) images of MWCNTs [1]. There was a period of lull

D. Casimir · R. Garcia-Sanchez · P. Misra (✉)
Department of Physics and Astronomy, Howard University, Washington, DC 20059, USA
e-mail: pmisra@howard.edu

P. Misra (ed.), *Applied Spectroscopy and the Science of Nanomaterials*,
Progress in Optical Science and Photonics 2, DOI 10.1007/978-981-287-242-5_1

regarding landmark discoveries relating to CNTs until 1976, when Oberlin et al. generated single- and multi-walled CNTs while trying to grow carbon fibers by pyrolyzing a mixture of benzene and hydrogen around 1,100 °C [2]. Such filamentous growth of carbon was followed by the observation of so-called carbon fibers in an arc discharge by Abrahamson, who reported this at the biennial carbon conference held at The Pennsylvania State University in 1979 and later reported their characterization in 1999 [3]. Circular shaped (armchair configuration) and helical shaped (chiral form) CNTs were suggested by Soviet scientists in 1982 following Transmission Electron Microscopy (TEM) imagery and X-ray Diffraction (XRD) pattern recording of carbon nanoparticles [4]. In 1987, Tennent received a U.S. patent for producing and characterizing the so-called carbon fibrils [5]. This was followed by Iijima's discovery of MWNTs in 1991, while attempting to understand the growth mechanisms associated with another carbon allotrope, namely buckminsterfullerene (or bucky-ball) [6] and Mintmire et al.'s publication in 1992 [7] regarding the promise of excellent conducting properties of fullerene tubules and their zero band gap at room temperature. Both Iijima and Mintmire et al.'s publications in the early 1990s helped bring significant visibility to CNTs and energized research into their characterization and properties at an astonishing pace all around the globe. Such investigations were spurred greatly by subsequent discoveries related to SWCNTs by Iijima and Iohihashi [8] and Bethune et al. [9].

Owing to their high aspect ratio, studies of CNTs can serve in testing theories of 1-dimensional systems [10]. Since being brought into the scientific spotlight over 20 years ago by Iijima [6], there have been rapid developments regarding the unique physical properties of CNTs and both SWCNTs and MWCNTs have been extensively studied. Investigations into their thermal properties serve as a good illustration of the continued interest in understanding both their behavior and the potential for a number of applications in materials science and engineering that arise from the wide-ranging configurations this material can take. Knowledge regarding the thermo-mechanical properties of CNTs, although not at presently limited, has often been controversial. One such topic lies in the axial and radial thermal expansions of SWCNTs. Kwon et al. [11] reported a negative thermal expansion of SWCNTs in a temperature interval of 0–800 K, while Li [12] reported positive values for the same temperature range. Optical techniques, such as fluorescence and Raman spectroscopy, allow rapid and reliable characterization of CNTs, including their structural imperfections and chirality.

The concept of chirality, or the ability to superpose the mirror image of an object on top of the original, is important for understanding the lattice and structural complexity of SWCNTs. SWCNTs can be grouped via two major classifications into chiral and achiral. By utilizing a folding construction on a flat graphene lattice, the primitive lattice of any SWCNT can be constructed based on the chiral and achiral classifications [13]. The axis of symmetry for SWCNTs is along the longitudinal direction, which in turn determines the arbitrary orientation and angle of the carbon hexagons along the cylindrical wall of the resulting nanotube. A surprisingly simple folding operation applied to the planar graphene lattice can account for the existence of only two achiral varieties (*armchair* and *zigzag*), and also for

the helicity of the remaining non-symmetric or chiral tube types. Also significant in this discussion is that the electronic properties of SWCNTs depend exclusively on their geometry [10]. However, it should be emphasized that the description regarding the nanotube structure is merely a mathematical construction, and that actual CNTs grow naturally in the form of cylinders according to complex and not fully understood growth mechanisms [14].

2 Electronic Structure of CNTs

Large-scale Atomic/Molecular Massively Parallel Simulator (LAMMPS) is an open source code that performs Molecular Dynamics (MD) simulations. By creating an input text file that specifies lattice spacing, atom type, atom interactions and other parameters of the nanoscale system we are trying to model, LAMMPS outputs a 'dump' file. This 'dump' file can be run by an MD visualization software, such as The Open Visualization Tool (Ovito) or Visual Molecular Dynamics (VMD) package. The visualization in Ovito shown in Fig. 1 shows a single sheet of graphene and the structure of the carbon atoms. Each atom is bonded to three other atoms forming the hexagonal shaped structure. With LAMMPS, the trajectories of atoms can be calculated and more complicated interactions can be simulated. Interestingly, for example, this structure could be extended to analyze water on graphene sheets.

LAMMPS utilizes four main components that need to be specified in each input text file, which are: *initialization*, *atom definition, settings* and *running simulations*. The 'initialization' dictates units, dimensions, atom styles, etc. For 2D graphene, the units are 'metal', and atom style is simply 'atomic'. The next step, atom definition, dictates the lattice spacing for graphene. A custom lattice is needed to

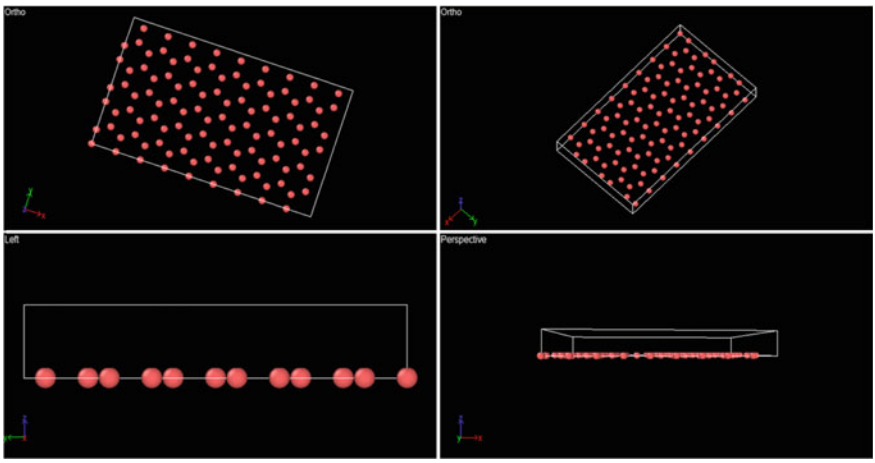

Fig. 1 3-D Visualization of graphene structure using the open visualization tool (*Ovito*) software

replicate the sheet of graphene (shown in Fig. 1). The distance between each atom was defined in angstroms based on literature values of lattice spacing for graphene [15]. The third section, settings, includes properties, such as pair and bond coefficients. This particular simulation required pair interactions, which can be defined as 'pair_style' under the atom definition section, and 'pair_coefficients' under settings. As a first approximation, one can use the Born potential for visualizing graphene; however, one needs to use the refined potential termed the Adaptive Intermolecular Reactive Empirical Bond Order (AIREBO) potential for a more accurate modeling and representation of the structure and its dynamics. Finally, a simulation can be set up for the molecules produced. Figure 1 shows the 3-D visualization generated for the structure of graphene employing a combination of LAMMPS and Ovito.

Let a_1 and a_2 be two graphene basis vectors, as illustrated in Fig. 2, and C_h the so-called chiral vector obtained as a linear combination of a_1 and a_2 in terms of a pair of integers n and m:

$$\boldsymbol{C_h} = n\boldsymbol{a}_1 + m\boldsymbol{a}_2 \tag{1}$$

with magnitude

$$|\boldsymbol{C_h}| = a\sqrt{n^2 + m^2 + nm} \tag{2}$$

where $|\boldsymbol{C_h}|$ can be considered as a measure of the circumference of the nanotube.

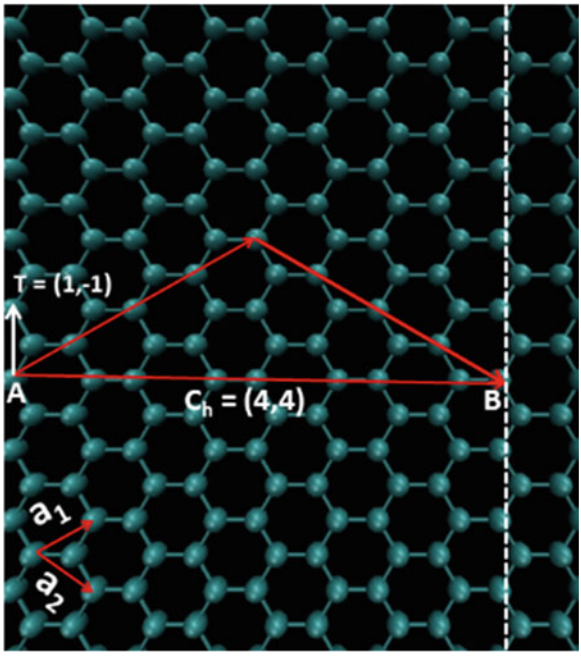

Fig. 2 Figure demonstrating the geometrical construction of a (4, 4) armchair single-walled carbon nanotube from a graphene sheet. The sheet is rolled along the chiral vector C_h until the Carbon atom at point A coincides with the Carbon atom at point B. The *rectangle* formed by the Translation vector T and the chiral vector form the unit cell of the resulting nanotube

The values of n and m are arbitrary with the constraint $0 \leq |m| \leq n$. The Cartesian components of the lattice vectors a_1 and a_2 are $(a\sqrt{3}/2, a/2)$ and $(a\sqrt{3}/2, -a/2)$, respectively, where $a = a_{C-C}\sqrt{3} = 2.46$ Å.

Figure 2 shows a diagram of a planar hexagonal lattice and the relevant geometrical parameters in the description of the conceptual rolling/folding operation in the construction of a single walled carbon nanotube from this sheet. The two vectors a_1 and a_2 are the basis lattice vectors of the planar sheet, and the vector is rolled along the chiral vector, C_h until point A coincides with point B. The first and second integers in the designation of the nanotube chirality n and m come from the amount of a_1 and a_2 vectors used to construct the two vectors that have the chiral vector as their resultant. The translation vector T, is the shortest possible vector that is perpendicular to the chiral vector that can be constructed from the basis vectors a_1, and a_2.

3 Thermo-Mechanical Properties of SWCNTs

It was anticipated in the 1990s when they were discovered that SWCNTs would have unique remarkable mechanical properties, and that has have proven to be the case. A common denominator among many of these extraordinary mechanical properties is the nature of the intra-planar Carbon-Carbon bond in the graphene lattice, the conceptual parent material of all other carbon allotropes including nanotubes. Overall, the mechanical properties of carbon nanotubes are reasonably well understood. However, research on these thermo-elastic properties is still not at a uniform level of development [11]. This is due to the fact that although continuum/elasticity theory has proven to be applicable in studying the mechanical properties of SWCNTs, its use at the nano-scale requires careful use. A major portion of the research of SWCNT mechanical properties concerns the measurement and calculation of various elastic constants, such as Poisson's ratio, Young's modulus, and the thermal expansion coefficients of bundled and individual SWCNTs.

Figure 3 shows an SEM image of a sample of the purified SWCNT reported on in this chapter and illustrates one of the exceptional mechanical properties of these objects hinted at above. SWCNTs were predicted to have rather "soft" surfaces for externally applied loads perpendicular to their axis, with the ability in some cases to flexibly bend around sharp corners or in circles and not break [1]. The relatively large free standing SWCNT imaged in the center of Fig. 3 shows just this behavior. In sp^2 graphitic materials the intra-planar covalent σ bonds from the base structure resulting in elastic thin film behavior along the axial direction for nanotubes. However, because SWCNTs have hollow cores with no interlayer potential interactions, perpendicular deformations, including unstable ones result in bending of the nanotube without any fracture of the base σ skeleton.

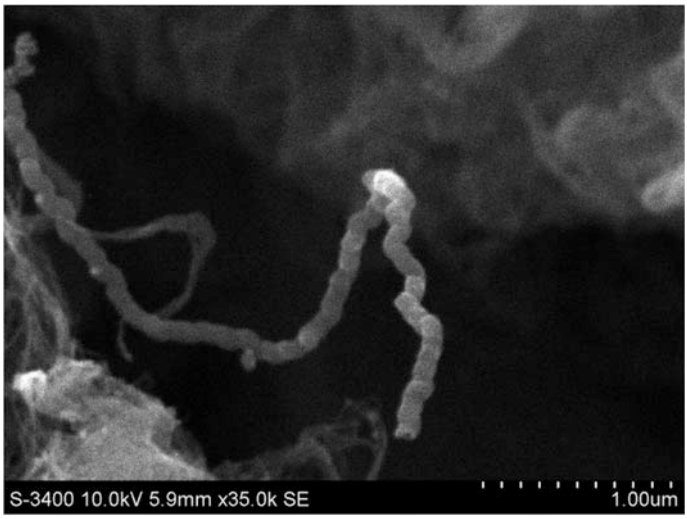

Fig. 3 SEM Image of purified SWCNT sample produced by the HiPco technique

4 Raman Spectroscopy of SWCNTs

We have used Raman spectroscopy for our experimental investigations into the thermal effects associated with SWCNTs. Resonance Raman spectroscopy serves as a sensitive tool for probing the mechanical properties of SWCNTs. Intensities of Raman transitions are typically quite weak, especially from the laser excitation of nano-sized entities, however the unique electronic properties of these quasi one dimensional objects cause a many fold increase in the Raman intensity, known as resonance Raman scattering, allowing in some cases for the collection of Raman spectra of individual SWCNTs.

A schematic of the instrument (Thermo Scientific DXR SmartRaman Spectrometer), employed to carry out the Raman spectroscopy measurements of the CNT samples, is shown in Fig. 4. A 780 nm laser source (frequency stabilized single mode diode with high brightness; frequency stability <1 cm^{-1} over a one-hour period and beam quality with a power setting of 6 mW was used. A full range grating was employed in the triplet spectrograph used (with an average spectral dispersion of 2 cm^{-1} per CCD pixel). The laser beam is focused on the sample using an objective lens and the scattered radiation from the sample is directed into the Imaging Spectrometer through a collection lens and a Raman signature (Stokes transitions only) is recorded using the appropriate Rayleigh filters and automated aperture (20–50 μm) selections as read by the CCD detector. Specifically, for instance, a 25 μm slit provided a resolution $\sim$1.93 cm^{-1}. A Ventacon Heated Cell served as a temperature-controlled environmental chamber (in the temperature range room temperature up to 200 °C) used and housed the sample either on its surface (in case of solid samples) or within (as in the case of nanopowders and

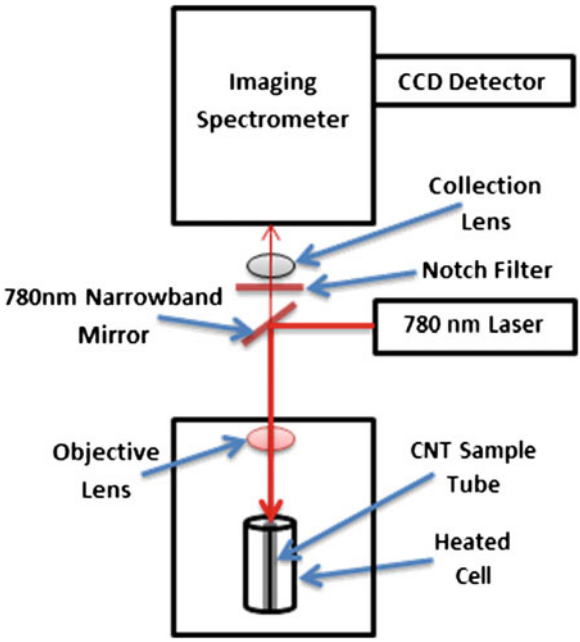

Fig. 4 A schematic of the experimental arrangement used for recording the Raman spectra of the CNT samples

carbon nanotubes). All temperature-dependent data were specifically collected for the purified batch of SWCNTs.

Significant Raman bands recorded for SWCNTs and their relationship to important mechanical properties are discussed below [16].

Figure 5 is an example Raman spectrum collected in the backscattering configuration with 780 nm laser excitation for a sample of SWCNTs produced through the high-pressure carbon monoxide (HiPco) process—a gas-phase method for large-scale production of CNTs—and subsequently purified to 15 % residual Fe catalyst by weight. The pair of peaks (labeled G^+ and G^-) are customarily present in sp^2-hybridized graphitic materials as a single peak characteristically identified as the G (Graphite)-band around $\sim$1,580 cm^{-1} and is related to the *in plane* C–C bond stretching mode for graphitic nanomaterials. Such (G^+ and G^-) peaks occur because of strain induced in rolled-up CNTS that cause the transverse and optical phonon modes to mix and become Raman active and subsequently split into two separate phonon frequency peaks—with peak separation serving as a direct measure of the amount of strain present in the graphitic nanomaterial being analyzed. (Both elasticity theory and ab initio techniques have been used in understanding how the above spectral features can also be linked to the diameters of the nanotubes.)

In Fig. 5, the splitting observed shows two peaks at 1559.88 and 1585.00 cm^{-1}, which correspond to G^- and G^+, respectively. These experimental results agree with the ab initio derived expression for G^- in Ref. [9].

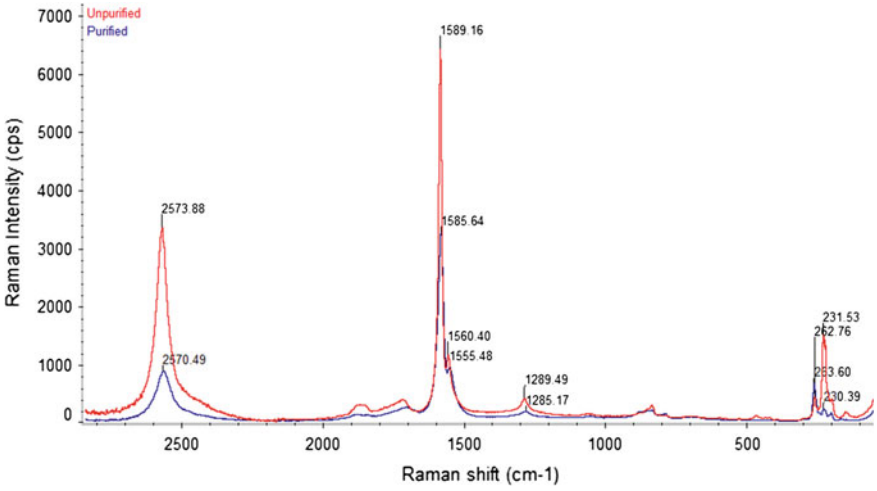

Fig. 5 Comparison of the Raman spectrum of both unpurified and purified SWCNT sample obtained with 780 nm excitation

$$\omega_G = 1592 - \frac{C}{d_t^{\beta}} \tag{3}$$

The experimental parameters obtained for this expression in Eq. (3) were as follows: $\beta = 1.4$, $C_{A1} = 41.4\ \text{cm}^{-1}\ \text{nm}$, $C_{E1} = 32.6\ \text{cm}^{-1}\ \text{nm}$, and $C_{E2} = 64.6\ \text{cm}^{-1}\ \text{nm}$ [9]. Small strain-induced changes in carbon nanotubes are easily measurable by Raman spectroscopy, due to the high frequency of the graphitic G band. For example, a mere 1 % strain-induced change in this Raman feature of sp^2-hybridized CNTs resulted in a measurable peak splitting $\sim 16\ \text{cm}^{-1}$, which is larger than the $10\ \text{cm}^{-1}$ width of the natural G band. The more than $25\ \text{cm}^{-1}$ difference between the two G band features for the semiconducting tubes in resonance, without any external loading, also exhibited this very useful feature of SWCNTs. The next group of bands in the low frequency regime, specifically the 264 and $228\ \text{cm}^{-1}$ features, dubbed the radial breathing modes (RBM), are another set of Raman features of SWCNTs that are intimately tied to their mechanical properties (like the previously discussed G band). However, where the G-band is present in all sp^2 graphitic materials, the RBM features are unique to nanotubes. As its name indicates, the RBM refers to the collective radial vibration of the SWCNT, as if it were breathing. This Raman feature is the one usually relied on for the estimation of the average diameter of CNTs, and not the diameter dependence of the G-band feature in Eq. (3). Both elasticity theory and ab initio techniques, in addition to experiment, predict an inverse diameter relationship for this Raman feature, with small deviations from the simple relationship given in Eq. (4) arising from effects due to inter-tube interactions in bundled nanotube samples and the Kohn anomaly.

$$\omega_{RBM} = \frac{A}{d_t} + B \tag{4}$$

In the present case, the pair of fitted parameters (A, B) used in the diameter estimation have the following values: A = 234 cm^{-1} nm and B = 10 cm^{-1}, yielding an average SWCNT diameter of ~1.09 nm for the 228.81 cm^{-1} Raman peak in Fig. 5. Based on the geometrical structure of SWCNTs described earlier, and Eq. (2), this diameter value can be shown to correlate to the specific chiralities (14, 0) and (10, 6). The RBM seen at 264.01 cm^{-1} is also of special interest. It has been shown in Ref. [10], based on an RBM intensity map with 785 nm excitation, that this peak is useful in assessing the extent of aggregation of the different tubes present in a bundled sample, which may prove to be another helpful technique in the ongoing search for simpler robust techniques in determining the diameter distribution of samples compared to scanning probe methods. This "roping" peak, present in the spectra in Fig. 5, corresponded to the chirality (10, 2)—being in resonance for bundled samples, while for individualized nanotubes a chirality of (12, 1) was the dominant one [10].

The two other labeled features in the Raman spectrum shown in Fig. 5 are the D (Defect) band at 1290.22 cm^{-1} and the 2D band at 2578.61 cm^{-1}, respectively. Although the intensity ratio of the D "Defect" band to the G band is used in assessing the quality of SWCNT samples, these results must be used cautiously as it is still uncertain if the D band can be used for defect characterization in all sp^2 hybridized nanocarbon materials. An important wrinkle is that the D band Raman feature of individual SWCNTs is narrow (with line-widths in the range of 7–40 cm^{-1}), and the Raman spectra of bundled samples are made up of broad peaks with superimposed features from separate nanotubes in a given graphitic nano-sample. Another issue is the lower frequency of the D band in SWCNTs, compared to other bulk sp^2 nanocarbons, and in addition the downshift of the D band in nanotubes is also diameter-dependent. In addition, the 2D band results of second-order scattering near the K-point in the planar graphene Brillouin zone occurs via a double resonance process and such a highly dispersive second order feature also proves useful in the characterization of SWCNTs.

Although the focus of the present report is single walled carbon nanotubes (SWCNTs), a sample Raman spectrum of multi walled carbon nanotubes (MWCNTs) is shown in Fig. 6 for comparison, and to illustrate the effectiveness in the use of Raman spectroscopy in the characterization of Carbon allotropes. The major differences between the two sets of spectra of MWCNT and SWCNT, respectively, are the reduction in intensity and the number of RBMs present in the multi-walled sample [17]. Also noticeable is the more prominent defect peak in the multi-walled carbon nanotube sample. The first effect is due to the restriction of the radial vibration by the outer walls of the nested coaxial nanotubes, and the latter effect has been attributed to the stacked multi-layer of MWCNTs leading to more opportunities for disorder [18].

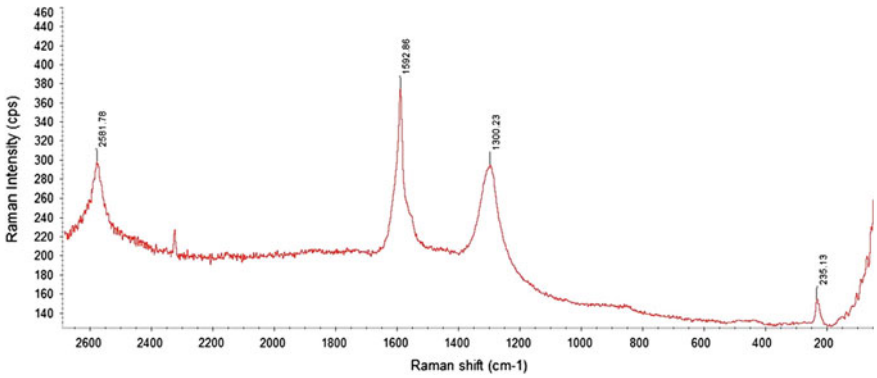

Fig. 6 Raman spectrum of multi walled carbon nanotubes with 780 nm laser excitation

4.1 Raman Spectra of SWCNTs as a Function of Temperature

When heated to higher temperatures the location of the Raman peaks of SWCNT and other carbon allotropes, shift to lower frequencies due to the softening of the inter-atomic bonds [18]. This red-shifting of the Raman frequencies of carbon nanotubes demonstrates the suitability of Raman spectroscopy in the characterization of carbon allotropes and carbon nanotubes in particular. This phenomenon can be decomposed into two effects, one purely thermal and the other a volume/strain effect caused by the thermal expansion of the crystal lattice. The first term in Eq. (5) represents the thermal effect, and the second term the volume effect [19].

$$\Delta\omega = \left(\frac{\partial\omega}{\partial T}\right)_V \Delta T + \left(\frac{\partial\omega}{\partial V}\right)_T \left(\frac{\partial V}{\partial T}\right)_P \Delta T \tag{5}$$

Many studies have shown however that the temperature effect is the dominant one in this phenomenon. For this reason both our results and those from the literature on this effect usually display a linear trend, since the second order term in Eq. (6) associated with the volume effect is usually very small [20].

$$\omega = \omega_0 - a_1 T - a_2 T^2 \tag{6}$$

Our results in reproducing the temperature induced linear red-shift of major Raman peaks in a sample of purified SWCNT ropes, specifically the G^+, G−, D, G′ and RBM peaks are shown in Figs. 7 and 8. Each data point on the plots is the average of two Raman spectra collected at the same sample point at each respective temperature. The linearity of the temperature variation of the G′ peak was not clearly evident in our data, with a significant amount of scattering in contrast to the other Raman peaks, as shown by its low coefficient of determination. The cause of

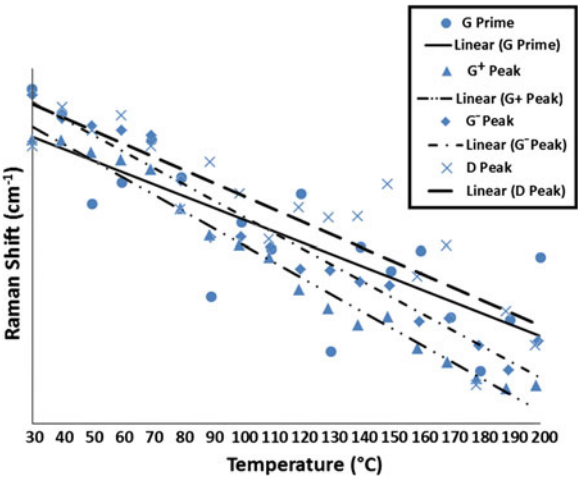

Fig. 7 The Raman Shift for the major SWCNT peaks as a function of temperature

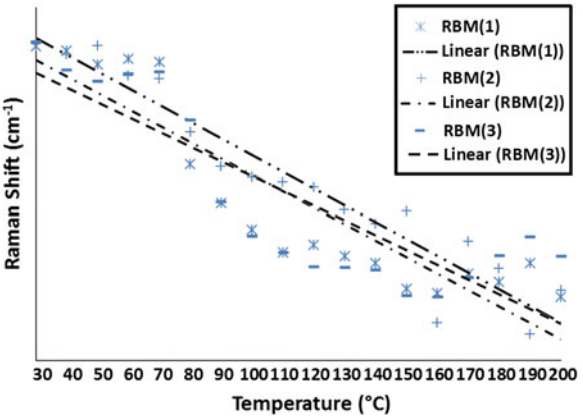

Fig. 8 The Raman Shift for the SWCNT RBM modes as a function of temperature

the departure from linearity in the redshift trend for this second order Raman band in our results is presently unknown. This peak however is very dispersive and sensitive to electronic and other perturbations [21]. This extreme sensitivity to thermal, mechanical and other perturbations was also the reason Deng et al., whose study is mentioned later also chose this Raman band in their thermal expansion study [22]. Raman spectral data were collected on the CNT samples under increasing temperature from room temperature up to 200 °C in 10 °C increments. The HiPco single walled nanotube samples were obtained from Unidym Carbon Nanotubes, and according to the manufacturer had only 15 % by weight of Fe catalyst present. The diameter range of the single walled carbon nanotubes was also stated as 0.8–1.2 nm [16].

Table 1 Values for the Raman shift (cm^{-1}) of the major SWCNT peaks with increasing temperature

Temp (°C)	G′	G^+	G	D	RBM (1)	RBM (2)	RBM (3)
30	2579.53	1594.2	1565.665	1294.405	267.58	233.995	206.425
40	2578.98	1594.19	1565.37	1294.96	267.555	233.935	206.28
50	2576.94	1594.055	1565.275	1294.625	267.475	233.985	206.225
60	2577.425	1593.97	1565.215	1294.845	267.51	233.815	206.2625
70	2578.375	1593.86	1565.155	1294.405	267.49	233.795	206.2725
80	2577.54	1593.42	1564.58	1293.52	266.91	233.495	206.0275
90	2574.86	1593.12	1563.86	1294.18	266.69	233.3	205.6075
100	2576.525	1593.015	1563.865	1293.735	266.54	233.24	205.4375
110	2575.925	1592.87	1563.74	1293.1	266.41	233.21	205.3525
120	2577.16	1592.51	1563.455	1293.545	266.455	233.18	205.28
130	2573.625	1592.3	1563.445	1293.4	266.39	233.055	205.2775
140	2575.975	1592.115	1563.3	1293.42	266.35	232.975	205.2625
150	2575.425	1592.205	1563.25	1293.875	266.205	233.045	205.1325
160	2575.88	1591.845	1562.795	1292.57	266.18	232.415	205.1275
170	2574.385	1591.69	1562.835	1293.005	266.29	232.875	205.225
180	2573.175	1591.51	1562.495	1291.04	266.245	232.725	205.3375
190	2574.335	1591.39	1562.18	1292.08	266.35	232.35	205.4325
200	2575.74	1591.43	1562.545	1291.6	266.16	232.6	205.335

Our tabulated and plotted results are shown in Figs. 7, 8, and Table 1, respectively, and the temperature slopes $\frac{\Delta\omega}{\Delta \mathbf{T}}$ presented in Table 2 agree well with Gregan [20] and Raravikar [23].

Raravikar [23] reported temperature slope $\left(\frac{\Delta\omega}{\Delta T}\right)$ values of −0.0189 and −0.0238 cm^{-1}/K for the G^+ and G^- peaks, respectively, using 514.4 nm excitation, while Gregan [20] reported similar values of −0.016 cm^{-1}/K for both G^+ and G^- peaks again using 514.5 nm excitation. In addition, in Table 2 we provide the temperature slopes for the G′, D and Radial Breathing Mode (RBM) features as well (with 780 nm excitation).

The temperature-shifted Raman peaks are useful in determining the thermal expansion coefficients associated with SWCNTs. It has been noted in the literature

Table 2 Temperature slopes of the various Raman peaks of bundled SWCNTs illustrated in Figs. 7 and 8

Raman band feature	Temperature slope $\frac{\Delta\omega}{\Delta T}$ (cm^{-1}/°C) using 780 nm excitation wavelength
G^+ Peak	−0.0187
G^- Peak	−0.0204
G′ Peak	−0.0264
"Defect" D Peak	−0.0182
RBM ~ 267 cm^{-1}	−0.0093
RBM ~ 234.31 cm^{-1}	−0.0095
RBM ~ 206.49 cm^{-1}	−0.0075

however, that the determination of the axial thermal expansion coefficient, and many other thermo-mechanical properties of individual carbon nanotubes is extremely difficult owing to their nanoscopic dimensions and also due to their appearance as one of many nanotubes entangled in complex nanotube bundles upon production (as illustrated in the SEM image shown in Fig. 3). Therefore, the majority of the values for the Coefficient of Thermal Expansion (CTE) coefficients are derived from experimental studies done on bundles of carbon nanotubes.

The latter is also true for the novel and practical recent work done by Deng et al. [22]. In Deng et al., the temperature shift in the Raman G′ band of single and double walled carbon nanotubes both in and outside of an epoxy mixture were measured. They chose to use the G′ band for the study because it, "was the most sensitive to external perturbations" [22]. The shift in the G′ band with applied strain with the laser polarization in the same direction as the applied strain was also measured, and finally using the temperature slope of the G′ band under the two previously mentioned conditions in addition to an average over all angular orientations of the strain shifted G` frequencies, Deng was able to calculate the CTE of the carbon nanotubes denoted as α_F in Eq. (7). α_E is the CTE of the epoxy matrix that the carbon nanotubes are embedded in Deng et al. [22].

$$\alpha_F = \alpha_E - {(\chi_C - \chi_F)}/{S_0} \tag{7}$$

Finally in this section, it is also shown that the thermal conductivity of SWCNTs can also be obtained through resonant Raman spectroscopy. Terekhov et al. [24] discusses a robust practical technique to estimate the thermal conductivity of a carbon nanotube sample. Initially while developing a Raman based calibration method of determining the amount of SWCNT content in powdered single walled carbon nanotube samples, they also noted the correlation between the temperature slope of the G^+ band of heated SWCNTs and the amount of SWCNT content present in the sample; using the above relationship, and the fact that the physical interpretation of the slope of the shift in the G^+ peak versus laser power density is the inverse thermal conductivity allowed them to estimate the thermal conductivity in samples with different amounts of SWCNT content or purity levels. Our reproduction of this technique, based on our data is shown in Fig. 9.

5 Molecular Dynamics Simulation

Computational studies regarding the mechanical properties of SWCNTs have often reported contradictory results for elastic moduli and constants. A major factor contributing to the above problem lies in the arbitrariness of the thickness of a nanotube shell, which is usually prescribed the value of the interlayer spacing in graphite $\sim$0.35 nm. The early computational studies of the elastic properties of SWCNTs usually ascribed to Robertson et al. [25] employed the Tersoff and

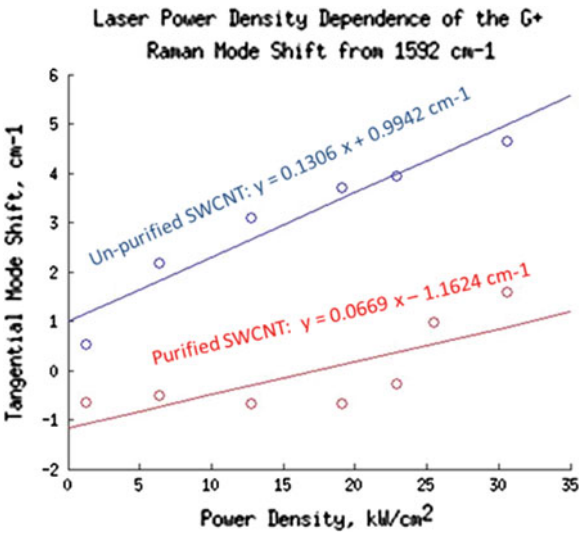

Fig. 9 The shift of the G^+ Raman feature away from 1,592 cm^{-1} upon heating caused by increased laser power density

Brenner empirical potentials, one of the first many-body empirical potentials used in such investigations. This particular study confirmed the elasticity theory-based prediction of the inverse squared diameter dependence of the strain energy, in addition to other interesting predictions, such as a decrease in the Young's modulus for extremely narrow SWCNTs. We have carried out Molecular Dynamics (MD) simulations based on the Adaptive Intermolecular Reactive Empirical Bond Order (AIREBO) potential [26, 27]. The latest iteration of the Tersoff-Brenner empirical potential, specifically developed for hydrocarbons, commonly in use now is the AIREBO potential:

$$E = \frac{1}{2}\sum_{i}\sum_{j\neq i}\left[E_{ij}^{REBO} + E_{ij}^{LJ} + \sum_{k\neq i,j}\sum_{l\neq i,j,k} E_{kijl}^{TORSION}\right] \tag{8}$$

The first term contains the repulsive and attractive interactions, including a special "bond order" term to modify bonded energies, the second term is the Lennard-Jones potential, and the last term calculates angular and torsional interactions. This potential was used to produce the illustrations in Figs. 10 and 11, a snapshot of one unit cell of a (12, 1) SWCNT representative of one of the chiralities present in the actual sample. Both figures are from equilibration runs, of MD simulations with 0.0005 ps time-steps, and a total of 80,000 time-steps. The bottom portion of Fig. 10 shows the distortion of a cross-sectional portion of the SWCNT during the first 3,000 time-steps in 1,000-step intervals. The choice of this empirical potential was also influenced by the extensive table of single-walled carbon nanotube mechanical properties produced by Bialoskorski and Rybicki using the above potential given in Eq. (8) [13].

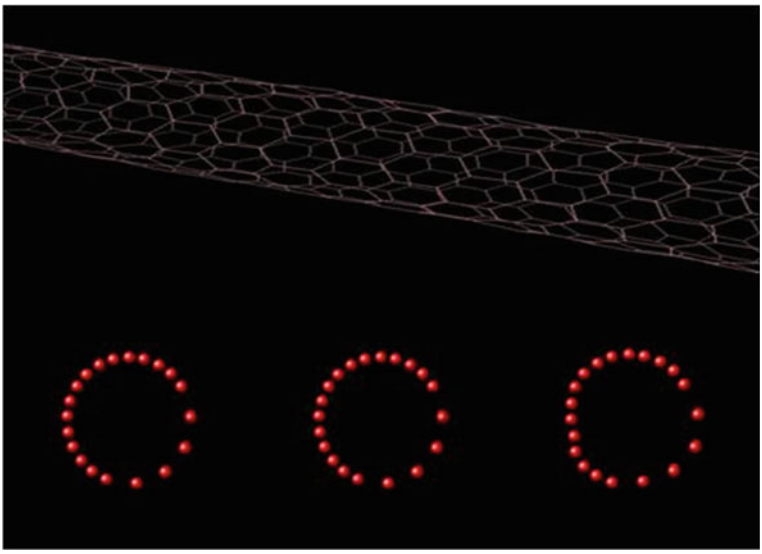

Fig. 10 Illustration of a (12, 1) chirality single-wall nanotube via molecular dynamics simulation using LAMMPS

Fig. 11 The axial sampling geometry of a SWCNT model based on Raman and Scanning Electron Microscope (SEM) analysis

Molecular Dynamics (MD) simulations examining the axial dimension denoted by the white arrow in Fig. 11 were also performed. This "apparent length" dimension, denoted by S, of the model carbon nanotube was constructed by separating the SWCNT into cylindrical sections 2 nm in height, and summing the center of mass distance between consecutive disks along the axial direction of the nanotube. Similar to the radial distortions, Verlet time integration with a 0.5 fs time step was used, and fixed boundary conditions employed in studying the distortion of this particular SWCNT dimension. MD simulations were performed at various temperatures in the range 100–800 K (in increments of 100 K). At each temperature, the apparent length behavior can be used to obtain the length of the SWCNT.

The apparent length variation of CNTs with temperature has been discussed by Cao et al. [28]. Our results also exhibit such variation. Figure 12, for instance, illustrates such variation of the axial dimension over the course of 100 ps during Nose-Hoover thermostated Molecular Dynamics (MD) simulation runs at 400 and 800 K.

Each sample point of the (apparent length) quantity S is the average of 10 samples selected every 100 time-steps, and averaged on every thousandth time-step.

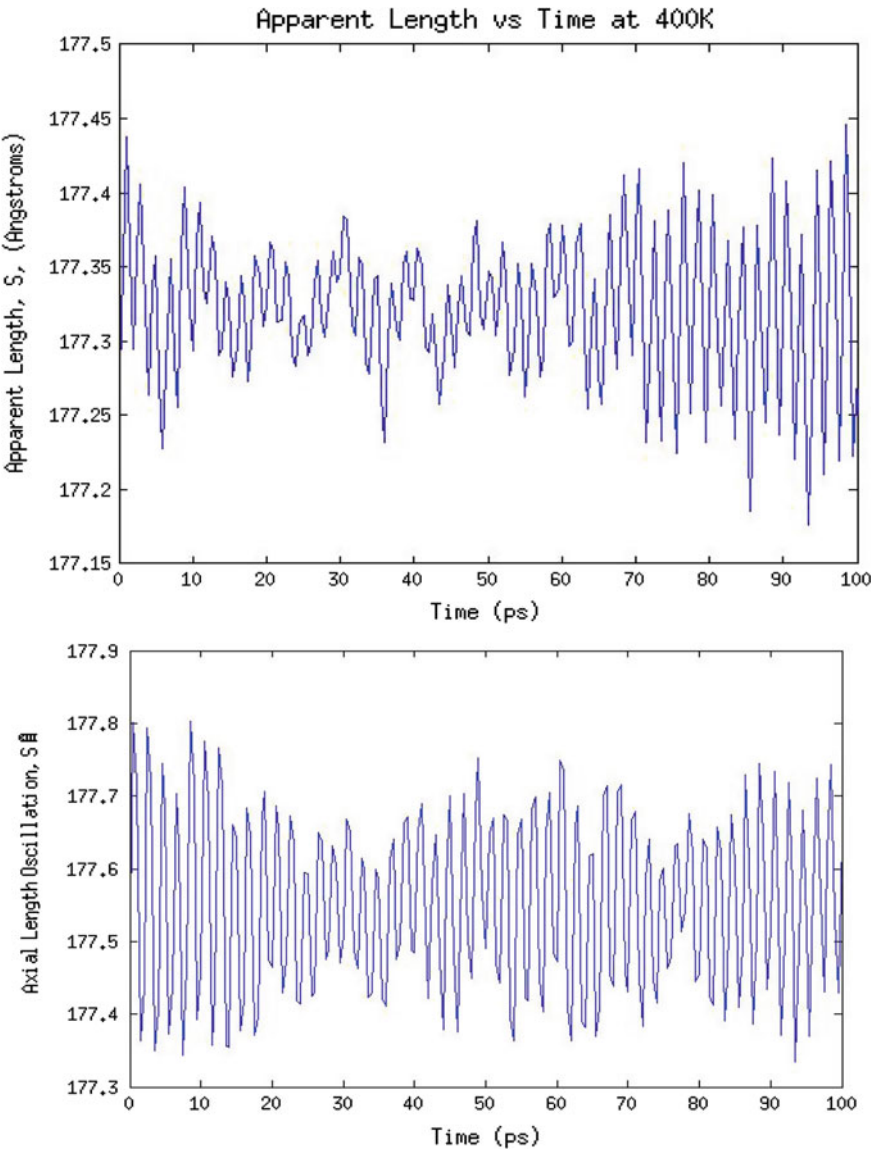

Fig. 12 Apparent length of SWCNTs versus time variation on the ps scale is shown in the plots for temperature runs of 400 and 800 K, respectively

Also, it needs to be noted that, before any sampling of the axial length S had begun, data from the first 100,000 time-steps of this quantity were discarded in order to allow time for thermal equilibrium. The oscillation of the apparent length S (shown in Fig. 12), appears to be a combination of low and high frequency vibration modes (akin to that reported by Cao et al. [28]).

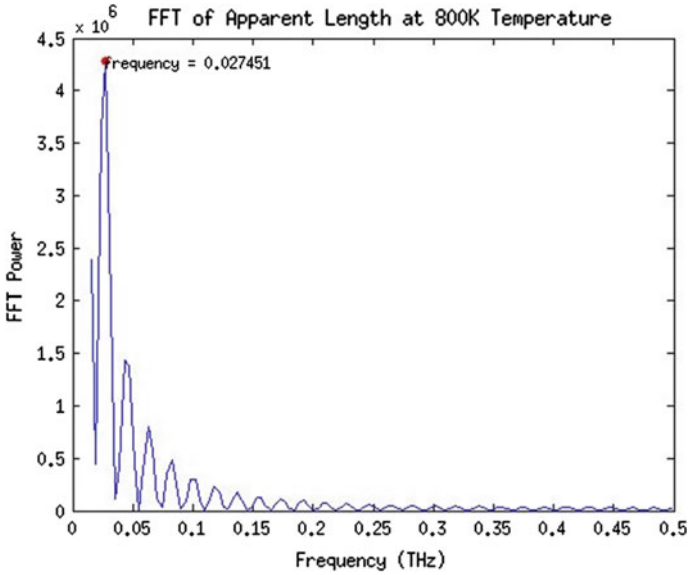

Fig. 13 Fast Fourier Transform (FFT) of the apparent length of SWCNTs at 800 K is illustrated as a FFT Power versus Frequency (in THz) plot

Figure 13 shows a discrete Fourier Transform of the axial length oscillation at a temperature of 800 K; it includes vibrations in both the longitudinal axial and transverse bending directions. Note that in this figure, only the dominant frequency at 0.027451 THz is labeled. As discussed in Cao et al. [28], this Fourier decomposition of the trajectory data obtained from Molecular Dynamics simulations is beneficial to the structural analysis of SWCNTs since it complements the predictions of continuum mechanics, wherein the nanotube is modeled as a smooth cylindrical shell made of an elastic homogeneous material.

6 Concluding Remarks

In this chapter we have discussed the history of carbon nanotube research and the remarkable properties they possess as a result of their varied electronic structure, which allows nanomaterials to have versatile electric and thermal properties [29, 30]. At the center of this versatility is the concept of chirality, which we can visualize by treating carbon nanotubes as if they were rolled-up sheets of graphene; rolling the graphene sheet around a chiral vector (whose direction and size are determined by the n and m chiral coefficients) results in a wide variety of carbon nanotube (n, m) configurations with metallic or semiconductor electrical properties and achiral or chiral structures.

The present chapter also discusses how Raman spectroscopy, a powerful optical technique, has been of increasing use in the study of the properties of nanomaterials.

With Raman spectroscopy, we can determine quantitatively the temperature shifts in frequency of the Raman peaks associated with carbon nanotubes. In addition, several researchers as cited above have shown significant amount of structural characterization based on thermal shifts of Raman spectral characteristics. Specifically, the use of the strain and temperature-induced frequency shift of the 2nd order G′ peak to obtain the axial thermal expansion coefficient was noted and discussed. We have also discussed the method of classical Molecular Dynamics simulation, and its application to the structural characterization of single-walled carbon nanotubes, with pertinent results and lucid demonstrations that compliment continuum based studies of the mechanical behavior of SWCNTs with data obtained from MD simulations. The useful ability to obtain an estimate of the thermal conductivity of SWCNT bundles via the temperature shift of the Raman G^+ mode under laser heating has also been demonstrated. Thanks in part to the electronic density of states of CNTs, Raman intensities are also enhanced several-fold, allowing for the identification of the Raman signal from de-bundled SWCNT samples. An important concept associated with the Raman spectroscopic studies of nanomaterials is the identification of the Raman peaks related to carbon allotropes, resulting in the important G, D and RBM Raman modes, which are used to determine a variety of significant mechanical and electrical properties of CNTs, including important differences between different types of CNTs, specifically, SWCNTs (purified and unpurified) and MWCNTs.

As shown in the reviews and the reported literature results summarized in the current chapter, much still remains to be done in the area of carbon nanotube characterization in general, and also specifically in our on-going investigations relating to thermal effects associated with CNTs. Regarding the latter, our Molecular Dynamics simulation results were primarily focused on the axial dimension of SWCNTs, and not on the radial dimension. Results on the latter based on our ongoing work are anticipated to yield an interesting dimension to the thermal characterization of SWCNTs. Also, the unique specific heat capacity of SWCNTs, the ability to determine the radial CTE of SWCNTs, and be able to probe their 1-dimensional characteristics, as discussed in [31], would add to greater understanding of the thermal behavior of CNTs and in their widespread applications.

Acknowledgments The authors would like to acknowledge the assistance of Ms. Larkin Sayre, a rising sophomore at the Massachusetts Institute of Technology (MIT) and a 2014 Summer Research Experiences for Undergraduates (REU) in Physics participant at Howard University (NSF Grant PHY-1358727), for generating Fig. 1.

References

1. Radushkevich LV, Lukyanovich VM (1952) Structure of the carbon produced in the thermal decomposition of carbon monoxide on an iron catalyst. Russ J Phys Chem 26:88–95
2. Oberlin A, Endo M, Koyama T (1976) Filamentous growth of carbon through benzene decomposition. J Cryst Growth 32:335–349
3. Abrahamson J, Wiles PG, Rhoades BL (1999) Structure of carbon fibers found on carbon arc anodes. Carbon 37(11): 1873

4. Nesterenko AM, Kolesnik NF, Akhmatov YuS, Suhomlin VI, Prilutskii OV (1982) Characteristics of the phase composition and structure of products of the interaction of nickel(II) and iron(III) oxide with carbon monoxide. Izevestiya Akadem ii Nauk, SSSR, Metals 3:12–17
5. Tennent HG (1987) Carbon fibrils, method for producing the same and compositions containing same. US Patent No. 4663230, 1987-05-05
6. Iijima S (1991) Helical microtubules of graphitic carbon. Nature 354:56–58
7. Mintmire JW, Dunlap BI, White CT (1992) Are fullerene tubules metallic? Phys Rev Lett 68:631
8. Iijima S, Iohihashi T (1993) Single-shell carbon nanotubes of 1-nm diameter. Nature 363 (6430):603–605
9. Bethune DS, Kiang CH, De Vries MS, Gorman G, Savoy R, Vazquez J, Beyers R (1993) Cobalt-catalyzed growth of carbon nanotubes with single-atomic—layer walls. Nature 363 (6430):605–607
10. Saito R, Dresselhauss G, Dresselhauss MS (1998) Physical properties of carbon nanotubes. Imperial College Press, London
11. Kwon YK, Berber S, Tomanek D (2004) Thermal contraction of carbon fullerenes and nanotubes. Phys Rev Lett 92:015901
12. Li C, Chan TW (2005) Axial and radial thermal expansions of single-walled carbon nanotubes. Phys Rev B 71:235414
13. Wong P, Akinwande D (2011) Carbon nanotube and graphene device physics. Cambridge University Press, Cambridge
14. Thess et al (1996) Crystalline ropes of metallic carbon Nanotubes. Science 273(5274): 483–487
15. Gray D, McCaughan A, MookerjCrystal B (2009) Structure of graphite, graphene and silicon. http://community.wvu.edu/∼mbh039/graphene.pdf. Accessed 14 Jun 2014
16. Misra P, Casimir D, Garcia-Sanchez R (2013) Thermal expansion properties of single-walled carbon nanotubes by raman spectroscopy at 780 nm wavelength. OPAP 2013 proceedings
17. O'Connell MJ, Sivaram S, Doorn SK (2004) Near-infrared resonance Raman excitation profile studies of single-walled carbon nanotube intertube interactions: a direct comparison of bundled and individually dispersed HiPco nanotubes. Phys Rev B 69:235415
18. Thermo scientific characterizing carbon with Raman. http://fscimage.thermoscientific.com/images/D19504∼.pdf. Accessed 14 Jun 2014
19. Dresselhaus MS, Eklund PC (2000) Phonons in carbon nanotubes. Adv Phys 49(6):705–814
20. Gregan E (2009) The use of raman spectroscopy in the characterization of single walled carbon nanotubes. Doctoral Dissertation, Dublin Institute of Technology, School of Physics
21. Jorio A, Saito R, Dresselhauss G, Dresselhauss MS (2011) Raman spectroscopy in graphene related systems. Wiley-VCH Verlag GmbH and Co, KGaA, Weinheim, Germany
22. Deng L, Young RJ, Kinloch IA, Sun R, Zhang G, Noe L, Monthioux M (2014) Coefficient of thermal expansion of carbon nanotubes measured by raman spectroscopy. Appl Phys Lett 104:051907
23. Raravikar et al (2002) Temperature dependence of radial breathing mode Raman frequency of single-walled carbon nanotubes. Phys Rev B 66:235424-1–235424-9
24. Terekhov SV, Obraztsova ED, Detltlaff-Weglikowska U, Roth S, Calibration of raman-based method for estimation of carbon nanotube purity. AIP Conf Proc 685:116
25. Robertson DH, Brenner DW, Mintmire JW (1992) Progress on mechanics of carbon nanotubes and derived materials. Phys Rev B 45:12592
26. Stuart SJ, Tutein AB, Harrison JA (2000) A reactive potential for hydrocarbons with intermolecular interactions. J Chem Phys 112:6472
27. Bialoskorski M, Rybicki J (2012) Mechanical properties of single-walled carbon nanotubes simulated with airebo force-field. Comp Meth Sci Tech 18(2):67–77
28. Cao G, Chen X, Kysar JW (2005) Apparent thermal contraction of single-walled carbon nanotubes. Phys Rev B 72:235404

29. Jorio A, Dresselhauss G, Dresselhauss MS (eds) (2008) Carbon nanotubes: advanced topics in the synthesis, structure, properties and applications. Springer, Berlin
30. Rao CNR, Subrahmanyan KS, Ramakrishna Matte HSS, Govindraj A (2011) Graphene: synthesis, functionalization and properties. Mod Phy Lett 25(7):427–451
31. Bagatskii MI, Barabashko MS, Dolbin AV, Sumarokov VV (2012) The specific heat and the radial thermal expansion of bundles of single-walled carbon nanotubes. Fiz Nizk Temp 38 (6):667–673